

Quantum transport in the cylindrical nanosize silicon-based MOSFET

S. N. Balaban^a, E. P. Pokatilov^a, V. M. Fomin^{a,b}, V. N. Gladilin^{a,b}, J. T. Devreese^b,
W. Magnus^c, W. Schoenmaker^c, M. Van Rossum^c, and B. Sorée^c

^a*Departamentul de Fizica Teoretică, Universitatea de Stat din Moldova,
MD-2009 Chişinău, Republica Moldova*

^b*Theoretische Fysica van de Vaste Stof, Universiteit Antwerpen (U.I.A.),
B-2610 Antwerpen, Belgium*

^c*IMEC, B-3001 Leuven, Belgium*

(May 11, 2019)

Abstract

A model is developed for a detailed investigation of the current flowing through a cylindrical nanosize MOSFET with a close gate electrode. The quantum mechanical features of the lateral charge transport are described by Wigner distribution function which is explicitly dealing with electron scattering due to acoustic phonons and acceptor impurities. A numerical simulation is carried out to obtain a set of I - V characteristics for various channel lengths. It is demonstrated that inclusion of the collision term in the numerical simulation is important for low values of the source-drain voltage. The calculations have further shown that the scattering leads to an increase of the electron density in the channel thereby smoothing out the threshold kink in I - V characteristics. An analysis of the electron phase-space distribution shows that scattering does not prevent electrons from flowing through the channel as a narrow stream, and that features of both ballistic and diffusive transport may be observed simultaneously.

I. INTRODUCTION

During the last decade significant progress has been achieved in the scaling of the metal-oxide-semiconductor field-effect transistor (MOSFET) down to semiconductor devices with nanometer sizes. In Ref. [1], the fabrication of silicon quantum wires with lengths and widths of about 60 nm and ~ 20 nm respectively is reported. The conductance of those quantum wires was measured for a wide range of temperatures, from 25 to 160 K. The fabrication and the investigation of a 40 nm gate length n-MOSFET are reported in Ref. [2]. The resulting nanosize n-MOSFET operates rather normally at room temperature. Using nanoimprint lithography, a field effect transistor (FET) with a 100 nm wire channel was fabricated [3] and the characteristics of this FET at room temperature were investigated. However, the small size of nanoscale MOSFET with a wide Si substrate negatively influences the device characteristics due to the floating body effect. Short channel effects together with random

effects in the silicon substrate are very well known to cause a degradation of the threshold voltage and the appearance of uncontrollable charge and current in regions far from the gate electrode. Therefore in a nanoscale conventional MOSFET, the controlling ability of the gate electrode is substantially weakened. Recently, considerable attention has been paid to SOI (Si-on-insulator) MOSFETs, which are prospective for creating new nanosize devices. In Refs. [4–6], a MOSFET with very thin SOI was theoretically investigated on the basis of a 2D analytical model, while in Ref. [7], a 1D model was used. Drain-induced barrier lowering was considered [4] and the physical mechanisms which determine the subthreshold slope (S-factor) were analyzed [5]. As a result, a substantial reduction of the short-channel effect in the SOI MOSFET as compared to that in the bulk devices was established. As was shown theoretically in Ref. [8], the use of a lightly doped source and drain leads to an increase of the effective channel length what allows one to weaken the drain-induced barrier lowering. In an SOI MOSFET with a Si-Ge source [9], an improved drain-to-source breakdown voltage is achieved due to the absorption of excess holes in the channel region. In a transistor device with a channel sandwiched between oxide layers (dual-gate MOSFET), the floating body effects are significantly suppressed [10]. A theoretical model of a dual-gate device is described in Ref. [11]. In Ref. [12] we have investigated the thermal equilibrium state of a nanoscale cylindrical silicon-based MOSFET device with a close gate electrode (MOSFETCGE). An advantage of the latter is the complete suppression of the floating body effect caused by external influences. Moreover, the short-channel effect in these devices can be even weaker than that in a dual-gate structure.

The main goal of the present work is the investigation of quantum transport in a nanosize MOSFETCGE device. We have developed a flexible 2D model which optimally combines analytical and numerical methods and describes the main features of the MOSFETCGE device. The theoretical modeling of the quantum transport features involves the use of the Wigner distribution function formalism [13–15]. The paper is organized as follows. In Section II, a description of the system is presented in terms of a one-electron Hamiltonian. In Section III the quantum Liouville equation satisfied by the electron density matrix is transformed into a set of one dimensional equations for partial Wigner distribution functions. A one-dimensional collision term is derived in Section IV. In Section V we describe a numerical model to solve the equations which have been derived for the partial Wigner distribution function. In Section VI the results of the numerical calculations are discussed. Finally, in Section VII we give a summary of our results and conclusions about the influence of the scattering processes in nanosize MOSFETs.

II. THE HAMILTONIAN OF THE SYSTEM

We consider a cylindrical nanosize MOSFETCGE structure (Fig. 1) described by cylindrical coordinates (r, ϕ, z) , where the z -axis is chosen to be the symmetry axis. In the semiconductor pillar the electron motion is determined by the following Hamiltonian

$$\hat{H}_j = -\frac{\hbar^2}{2m_j^\perp} \frac{\partial^2}{\partial^2 \mathbf{r}_\perp} - \frac{\hbar^2}{2m_j^\parallel} \frac{\partial^2}{\partial^2 z} + V(\mathbf{r}), \quad (1)$$

where $V(\mathbf{r}) = V_b(\mathbf{r}) + V_e(\mathbf{r})$ is the potential energy associated with the energy barrier and the electrostatic field, respectively; m_j^\perp and m_j^\parallel are the effective masses of the transverse (in

(x, y)-plane) and longitudinal (along z -axis) motion of an electron of the j -th valley.

The electrostatic potential energy $V_e(\mathbf{r})$ satisfies Poisson's equation

$$\Delta V_e(\mathbf{r}) = \frac{e^2}{\varepsilon_0 \varepsilon_i} (-n(\mathbf{r}) + N_D(\mathbf{r}) - N_A(\mathbf{r})), \quad i = 1, 2, \quad (2)$$

where ε_1 and ε_2 are the dielectric constants of the semiconductor and oxide layers, respectively; $n(\mathbf{r})$, $N_D(\mathbf{r})$ and $N_A(\mathbf{r})$ are the concentrations of electrons, donors and acceptors respectively. In our calculations we assume that the source electrode is grounded whereas the potentials at the drain and gate electrodes are equal V_{ds} and V_G , respectively.

The study of the charge distribution in the cylindrical nanosize MOSFETCGE structure in the state of the thermodynamical equilibrium (see Ref. [12]) has shown that the concentration of holes is much lower than that of electrons so that electron transport is found to provide the main contribution to the current flowing through the MOSFET. For that reason, holes are neglected in the present transport calculations.

III. THE LIOUVILLE EQUATION

In this section we consider ballistic transport of electrons. Neglecting scattering processes and inter-valley transitions in the conduction band, the one-electron density matrix can be written as

$$\rho(\mathbf{r}, \mathbf{r}') = \sum_j \rho_j(\mathbf{r}, \mathbf{r}'), \quad (3)$$

where $\rho_j(\mathbf{r}, \mathbf{r}')$ is the density matrix of electrons residing in the j -th valley satisfying Liouville's equation

$$i\hbar \frac{\partial \rho_j}{\partial t} = [H_j, \rho_j]. \quad (4)$$

In order to impose reasonable boundary conditions for the density matrix in the electrodes, it is convenient to describe the quantum transport along the z -axis in a phase-space representation. In particular, we rewrite Eq. (4) in terms of $\zeta = (z + z')/2$ and $\eta = z - z'$ coordinates and express the density matrix ρ_j as

$$\rho_j(\mathbf{r}, \mathbf{r}') = \sum_{ms, m's'} \frac{1}{2\pi} \int_{-\infty}^{+\infty} dk e^{ik\eta} f_{jmsm's'}(\zeta, k) \Psi_{jms}(\mathbf{r}_\perp, z) \Psi_{jm's'}^*(\mathbf{r}'_\perp, z'), \quad (5)$$

with a complete set of orthonormal functions $\Psi_{jms}(\mathbf{r}_\perp, z)$. According to the cylindrical symmetry of the system, these functions take the following form:

$$\Psi_{jms}(\mathbf{r}_\perp, z) = \frac{1}{\sqrt{2\pi}} \psi_{jms}(r, z) e^{im\phi}. \quad (6)$$

The functions $\psi_{jms}(r, z)$ are chosen to satisfy the equation

$$-\frac{\hbar^2}{2m_j} \left[\frac{1}{r} \frac{\partial}{\partial r} \left(r \frac{\partial}{\partial r} \right) - \frac{m^2}{r^2} \right] \psi_{jms}(r, z) + V(r, z) \psi_{jms}(r, z) = \mathcal{E}_{jms}(z) \psi_{jms}(r, z), \quad (7)$$

which describes the radial motion of an electron. Here $\mathcal{E}_{jms}(z)$ are the eigenvalues of Eq. (7) for a given value of the z -coordinate which appears as a parameter. It will be shown, that $\mathcal{E}_{jms}(z)$ plays the role of an effective potential in the channel, and that $\Psi_{jms}(\mathbf{r}_\perp, z)$ is the corresponding wavefunction of the transverse motion at fixed z . Substituting the expansion (5) into Eq. (4), and using Eq. (7), we arrive at an equation for $f_{jmsm's'}(\zeta, k)$:

$$\begin{aligned} \frac{\partial f_{jmsm's'}(\zeta, k)}{\partial t} = & -\frac{\hbar k}{m_j^\parallel} \frac{\partial}{\partial \zeta} f_{jmsm's'}(\zeta, k) + \frac{1}{\hbar} \int_{-\infty}^{+\infty} W_{jmsm's'}(\zeta, k-k') f_{jmsm's'}(\zeta, k') dk' \\ & - \sum_{s_1, s_1'} \int_{-\infty}^{+\infty} \hat{M}_{jmsm's'}^{s_1 s_1'}(\zeta, k, k') f_{jms_1 m' s_1'}(\zeta, k') dk', \end{aligned} \quad (8)$$

where

$$W_{jmsm's'}(\zeta, k-k') = \frac{1}{2\pi i} \int_{-\infty}^{+\infty} (\mathcal{E}_{jms}(\zeta + \eta/2) - \mathcal{E}_{jms'}(\zeta - \eta/2)) e^{i(k'-k)\eta} d\eta, \quad (9)$$

$$\hat{M}_{jmsm's'}^{s_1 s_1'}(\zeta, k, k') = \frac{1}{2\pi} \int_{-\infty}^{+\infty} [\delta_{s's_1} \hat{\Gamma}_{mss_1}(\zeta + \eta/2, k') + \delta_{ss_1} \hat{\Gamma}_{ms's_1}^*(\zeta - \eta/2, k')] e^{i(k'-k)\eta} d\eta, \quad (10)$$

$$\hat{\Gamma}_{mss_1}(z, k') = \frac{\hbar}{2m_j^\parallel i} b_{jms_1}(z) + \frac{\hbar}{2m_j^\parallel} c_{jms_1}(z) \left(-i \frac{\partial}{\partial \zeta} + 2k' \right), \quad (11)$$

and

$$b_{jms_1}(z) = \int \psi_{jms}^*(r, z) \frac{\partial^2}{\partial z^2} \psi_{jms_1}(r, z) r dr, \quad (12)$$

$$c_{jms_1}(z) = \int \psi_{jms}^*(r, z) \frac{\partial}{\partial z} \psi_{jms_1}(r, z) r dr. \quad (13)$$

Note that Eq. (8) is similar to the Liouville equation for the Wigner distribution function, which is derived to model quantum transport in tunneling diodes (see Ref. [13]). The first drift term in the right-hand side of Eq. (8) is derived from the kinetic-energy operator of the longitudinal motion. It is exactly the same as the corresponding term of the Boltzmann equation. The second component plays the same role as the force term does in the Boltzmann equation. The last term in the right-hand side of Eq. (8) contains the operator $\hat{M}_{jmsm's'}^{s_1 s_1'}(\zeta, k, k')$, which mixes the functions $f_{jmsm's'}$ with different indexes s, s' . It appears because $\psi_{jms}(r, z)$ are not eigenfunctions of the Hamiltonian (1). The physical meaning of the operator $\hat{M}_{jmsm's'}^{s_1 s_1'}(\zeta, k, k')$ will be discussed below.

In order to solve Eq. (8), we need to specify boundary conditions for the functions $f_{jmsm's'}(\zeta, k)$. For a weak current, electrons incoming from both the source and the drain electrodes, are assumed to be maintained in thermal equilibrium. Comparing Eq. (5) with the corresponding expansion of the density matrix in the equilibrium state, one obtains the following boundary conditions

$$\begin{aligned}
f_{jmsm's'}(0, k) &= \delta_{ss'}\delta_{mm'}2 [\exp(E_{j_{smk}}\beta - E_{FS}\beta) + 1]^{-1}, & k > 0, \\
f_{jmsm's'}(L, k) &= \delta_{ss'}\delta_{mm'}2 [\exp(E_{j_{smk}}\beta - E_{FD}\beta) + 1]^{-1}, & k < 0,
\end{aligned} \tag{14}$$

where the total energy is $E_{j_{smk}} = \hbar^2 k^2 / 2m_j^{\parallel} + \mathcal{E}_{j_{sm}}(0)$ for an electron entering from the source electrode ($k > 0$) and $E_{j_{smk}} = \hbar^2 k^2 / 2m_j^{\parallel} + \mathcal{E}_{j_{sm}}(L)$ for an electron entering from the drain electrode ($k < 0$). E_{FS} and E_{FD} are the Fermi energy levels in the source and in the drain, respectively. Note, that Eq. (14) meets the requirement of imposing only one boundary condition on the function $f_{jmsm's'}(\zeta, k)$ at a fixed value of k as Eq. (8) is a first order differential equation with respect to ζ . Generally speaking, the solution of Eq. (8) with the conditions (14) depends on the distance between the boundary position and the active device region. Let us estimate how far the boundary must be from the active device region in order to avoid this dependence. It is easy to show that the density matrix of the equilibrium state is a decaying function of $\eta = z - z'$. The decay length is of the order of the coherence length $\lambda_T = \sqrt{\frac{\hbar^2}{m_j^{\parallel} k_B T}}$ at high temperature and of the inverse Fermi

wavenumber $k_F^{-1} = \sqrt{\hbar^2 / 2m_j^{\parallel} E_F}$ at low temperature. So, it is obvious, that the distance between the boundary and the channel must exceed the coherence length or the inverse Fermi wavenumber, i. e. $L \gg \lambda_T$ or $L \gg k_F^{-1}$. For example, at $T = 300$ K the coherence length $\lambda_T \sim 3$ nm is much less than the source or drain lengths.

The functions $f_{jmsm's'}(\zeta, k)$, which are introduced in Eq. (5), are used in calculations of the current and the electron density. The expression for the electron density follows directly from the density matrix as $n(\mathbf{r}) = \rho(\mathbf{r}, \mathbf{r})$. In terms of the functions $f_{jmsm's'}(\zeta, k)$, the electron density can be written as follows:

$$n(\mathbf{r}) = \frac{1}{2\pi} \sum_{jmsm's'} \int_{-\infty}^{+\infty} f_{jmsm's'}(z, k) dk \Psi_{jms}(\mathbf{r}_{\perp}, z) \Psi_{jm's'}^*(\mathbf{r}_{\perp}, z). \tag{15}$$

It is well-known [16], that the current density can be expressed in terms of the density matrix

$$\mathbf{j}(\mathbf{r}, t) = \sum_j \frac{e\hbar}{2m_j i} \left(\frac{\partial}{\partial \mathbf{r}} - \frac{\partial}{\partial \mathbf{r}'} \right) \rho_j(\mathbf{r}, \mathbf{r}', t) \Big|_{\mathbf{r}=\mathbf{r}'}. \tag{16}$$

The total current, which flows through the cross-section of the structure at a point z , can be obtained by an integration over the transverse coordinates. Substituting the expansion (5) into Eq. (16) and integrating over r and φ , we find

$$J = e \sum_{j,m,s} \frac{1}{2\pi} \int_{-\infty}^{+\infty} dk \frac{\hbar k}{m_j^{\parallel}} f_{jmsms'}(z, k) - \frac{2e\hbar}{m_j^{\parallel}} \sum_{\substack{j,m,s,s' \\ s' > s}} c_{jms's'}(z) \int_{-\infty}^{+\infty} dk \text{Im} f_{jmsms'}(z, k), \tag{17}$$

where $\text{Im} f$ is the imaginary part of f . The first term in the right-hand side of Eq. (17) is similar to the expression for a current of the classical theory [16]. The second term, which depends on the non-diagonal functions $f_{jmsms'}$ only, takes into account the effects of intermixing between different states of the transverse motion.

The last term in the right-hand side of Eq. (8) takes into consideration the variation of the wavefunctions $\psi_{jms}(r, z)$ along the z -axis. In the source and drain regions, the electrostatic

potential is essentially constant due to the high density of electrons. In these parts of the structure, the wavefunctions of the transverse motion are very weakly dependent on z , and consequently, the operator $\hat{M}_{jmsm's'}^{s_1s'_1}$ has negligible effect. Inside the channel, electrons are strongly localized at the Si/SiO₂ interface as the positive gate voltage is applied. Earlier calculations, which we made for the case of equilibrium [12], have shown that in the channel the dependence of $\psi_{jms}(r, z)$ on z is weak, too. Therefore, in the channel the effect of the operator $\hat{M}_{jmsm's'}^{s_1s'_1}$ is negligible. In the intermediate regions (the source–channel and the drain–channel), an increase of the contribution of the third term in the right-hand side of Eq. (8) is expected due to a sharp variation of $\psi_{jms}(r, z)$. Since $\hat{M}_{jmsm's'}^{s_1s'_1}$ couples functions $f_{jmsm's'}(\zeta, k)$ with different quantum numbers (jms), it can be interpreted as a collision operator, which describes transitions of electrons between different quantum states of the transverse motion. Thus, the third term in the right-hand side of Eq. (8) is significant only in the close vicinity of the p-n junctions. Therefore, this term is assumed to give a small contribution to the charge and current densities. Under the above assumption, we have treated the last term in the right-hand side of Eq. (steady state of the system in a zeroth order approximation with respect to the operator $\hat{M}_{jmsm's'}^{s_1s'_1}$. Neglecting the latter, one finds that, due to the boundary conditions (14), all non-diagonal functions $f_{jmsm's'}(\zeta, k)$ ($m \neq m'$ or $s \neq s'$) need to be zero.

In the channel, the energy of the transverse motion can be approximately written in the form [12]

$$\mathcal{E}_{jms}(z) = \mathcal{E}_{js}(z) + \frac{\hbar^2 m^2}{2m_{js}^\perp R_{js}^{*2}}, \quad (18)$$

where $\mathcal{E}_{js}(z)$ is the energy associated with the radial size quantization and $\hbar^2 m^2 / 2m_{js}^\perp R_{js}^{*2}$ is the energy of the angular motion with averaged radius R_{js}^* . Hence, in Eq. 9 for the diagonal functions $f_{jmsms}(\zeta, k)$ the difference $\mathcal{E}_{jms}(\zeta + \eta/2) - \mathcal{E}_{jms}(\zeta - \eta/2)$ can be substituted by $\mathcal{E}_{js}(\zeta + \eta/2) - \mathcal{E}_{js}(\zeta - \eta/2)$. Furthermore, summation over m in Eq. (8) gives

$$\frac{\hbar k}{m_j^\parallel} \frac{\partial}{\partial \zeta} f_{js}(\zeta, k) - \frac{1}{\hbar} \int_{-\infty}^{+\infty} W_{js}(\zeta, k - k') f_{js}(\zeta, k') dk' = 0 \quad (19)$$

with

$$f_{js}(\zeta, k) = \frac{1}{2\pi} \sum_m f_{jmsms}(\zeta, k). \quad (20)$$

In Eq. (19) the following notation is used

$$W_{js}(\zeta, k) = -\frac{1}{2\pi} \int_{-\infty}^{+\infty} (\mathcal{E}_{js}(\zeta + \eta/2) - \mathcal{E}_{js}(\zeta - \eta/2)) \sin(k\eta) d\eta. \quad (21)$$

The effective potential $\mathcal{E}_{js}(z)$ can be interpreted as the bottom of the subband (j, s) in the channel. The function $f_{js}(\zeta, k)$ is referred to as a partial Wigner distribution function describing electrons which are travelling through the channel in the inversion layer subband (j, s).

IV. ELECTRON SCATTERING

In this section we consider the electron scattering from phonons and impurities. For this purpose we introduce a Boltzmann-like single collision term [16], which in the present case has the following form

$$St f_{jsmk} = \sum_{j's'm'k'} (P_{jsmk,j's'm'k'} f_{j's'm'k'} - P_{jsmk,j's'm'k'} f_{jsmk}). \quad (22)$$

As was noted above, we have neglected all transitions between quantum states with different sets of quantum numbers j and s . In the source and drain contacts the distribution of electrons over the quantum states of the angular motion corresponds to equilibrium. Consequently, due to the cylindrical symmetry of the system, we may fairly assume that across the whole structure the electron distribution is given by

$$f_{jsmk}(z) = f_{js}(z, k) w_{jsm}, \quad (23)$$

where

$$w_{jsm} = \sqrt{\frac{\hbar^2 \beta}{2m_j^\perp R_{js}^2 \pi}} \exp\left(-\frac{\beta \hbar^2 m^2}{2m_j^\perp R_{js}^2}\right) \quad (24)$$

is the normalized Maxwellian distribution function with respect to the angular momentum m . The integration of the both sides of Eq. (22) over the angular momentum gives the one-dimensional collision term

$$St f_{js}(z, k) = \sum_{k'} (P_{js}(k, k') f_{js}(z, k') - P_{js}(k', k) f_{js}(z, k)), \quad (25)$$

where

$$P_{js}(k, k') = \sum_{mm'} P_{jsmk, js m' k'} w_{js m'}. \quad (26)$$

This collision term is directly incorporated into the one-dimensional Liouville equation (19) as

$$\tilde{W}_{js}(z, k, k') = W_{js}(z, k - k') + P_{js}(z, k, k') - \delta_{k,k'} \sum_{k'} P_{js}(z, k', k), \quad (27)$$

where $\tilde{W}_{js}(z, k, k')$ is the modified force term in Eq. (19).

In this work we consider scattering by acceptor impurities and acoustic phonons described by a deformation potential. The scattering rates are evaluated according to Fermi's golden rule

$$P_{jsmk, js m' k'} = \frac{2\pi}{\hbar} |\langle js m' k' | \hat{H}_{int} | js m k \rangle|^2 \delta(E_{js m' k'} - E_{js m k}), \quad (28)$$

where \hat{H}_{int} is the Hamiltonian of the electron-phonon or the electron-impurity interaction. Hereafter, we model the potential of an ionized acceptor as $U(\mathbf{r}) = 4\pi e^2 R_s^2 / \varepsilon_1 \delta(\mathbf{r})$, where R_s

determines a cross-section for scattering by an impurity. Consequently, the absolute value of the matrix element is

$$|\langle jsm'k' | U(\mathbf{r} - \mathbf{r}_i) | jsmk \rangle| = 4\pi e^2 R_s^2 / \varepsilon_1 \psi_{js}^2(r_i, z_i). \quad (29)$$

Averaging this over a uniform distribution of acceptors results in the following scattering rate

$$P_{jsmk, jsm'k'}^i = C_i \int_0^R \psi_{js}^4(r, z) \delta(E_{jsm'k'} - E_{jsmk}) r dr, \quad (30)$$

where $C_i = N_a (4\pi e^2 R_s^2 / \varepsilon_1)^2 / \hbar$ and N_a is the acceptor concentration.

At room temperature the rate of the scattering by acoustic phonons has the same form. Indeed, for $T = 300$ K the thermal energy $k_B T \gg \hbar \omega_{\mathbf{q}}$, therefore the acoustic deformation potential scattering is approximately elastic, and the emission and absorption rates are equal to each other. For low energies we can approximate the phonon number as $N_{\mathbf{q}} \approx k_B T / \hbar \omega_{\mathbf{q}} \gg 1$ and the phonon frequency $\omega_{\mathbf{q}} = v_0 q$, where v_0 is the sound velocity. Assuming equipartition of energy in the acoustic modes, the scattering rate is

$$P_{jsmk, jsm'k'}^{ph} = \frac{2\pi}{V} C_{ph} \sum_{\mathbf{q}} |\langle jsm'k' | e^{i\mathbf{q}\cdot\mathbf{r}} | jsmk \rangle|^2 \delta(E_{jsm'k'} - E_{jsmk}), \quad (31)$$

where the parameter $C_{ph} = 4\Sigma^2 k_B T / 9\pi \rho v_0^2 \hbar$. Integrating over \mathbf{q} yields the scattering rate $P_{jsmk, jsm'k'}^{ph}$ in the form (30) with C_{ph} instead of C_i . The full scattering rate $P_{jsmk, jsm'k'} = P_{jsmk, jsm'k'}^i + P_{jsmk, jsm'k'}^{ph}$ is then inserted into Eq. (26) in order to obtain the one-dimensional scattering rate

$$P_{js}(z, k, k') = (C_i + C_{ph}) a(z) F \left(\frac{\hbar^2 k'^2}{2m_j^{\parallel}} - \frac{\hbar^2 k^2}{2m_j^{\parallel}} \right), \quad (32)$$

where

$$a(z) = \sqrt{\frac{2m_j^{\perp}}{\hbar^2 \pi \beta}} R_{js}(z) \int_0^R \psi_{js}^4(r, z) r dr, \quad F(x) = e^{-x/2} K_0(|x|/2),$$

where $K_0(x)$ is a McDonald function [17]. In calculations of the scattering by acoustic phonons the following values of parameters for Si are used: $\Sigma = 9.2$ eV, $\rho = 2.3283 \cdot 10^3$ kg/m³, $v_0 = 8.43 \cdot 10^5$ cm/s [18]

V. NUMERICAL MODEL

The system under consideration consists of regions with high (the source and drain) and low (the channel) concentrations of electrons. The corresponding electron distribution difference would produce a considerable inaccuracy if we would have attempted to directly construct a finite-difference analog of Eq. (19). It is worth mentioning that, in the quasi-classical limit, i. e. $\mathcal{E}_{js}(\zeta + \eta/2) - \mathcal{E}_{js}(\zeta - \eta/2) \approx \frac{\partial \mathcal{E}_{js}(\zeta)}{\partial \zeta} \eta$, Eq. (19) leads to the Boltzmann

equation with an effective potential which has the following exact solution in the equilibrium state:

$$f_{js}^{eq}(\zeta, k) = \frac{1}{\pi} \sum_m \left[\exp \left(\frac{\hbar^2 k^2}{2m_j^{\parallel}} \beta + \mathcal{E}_{j,s}(\zeta) \beta + \frac{\hbar^2 m^2 \beta}{2m_{js}^{\perp} R_{js}^{*2}(\zeta)} - E_F \beta \right) + 1 \right]^{-1} \quad (33)$$

For numerical calculations it is useful to write down the partial Wigner distribution function as $f_{js}(\zeta, k) = f_{js}^{eq}(\zeta, k) + f_{js}^d(\zeta, k)$. Inserting this into Eq. (19), one obtains the following equation for $f_{js}^d(\zeta, k)$:

$$\frac{\hbar k}{m_j^{\parallel}} \frac{\partial}{\partial \zeta} f_{js}^d(\zeta, k) - \frac{1}{\hbar} \int_{-\infty}^{+\infty} W_{js}(\zeta, k - k') f_{js}^d(\zeta, k') dk' = B_{js}(\zeta, k), \quad (34)$$

where

$$B_{js}(\zeta, k) = \frac{1}{2\pi} \int_{-\infty}^{+\infty} dk' \int_{-\infty}^{+\infty} d\eta \left(\mathcal{E}_{j,s}(\zeta + \frac{\eta}{2}) - \mathcal{E}_{j,s}(\zeta - \frac{\eta}{2}) - \frac{\partial \mathcal{E}_{j,s}(\zeta)}{\partial \zeta} \eta \right) \sin [(k - k')\eta] f_{js}^{eq}(\zeta, k'). \quad (35)$$

The unknown function $f_{js}^d(\zeta, k)$ takes values of the same order throughout the whole system, and therefore is suitable for numerical computations. In the present work, we have used the finite-difference model, which is described in Ref. [13]. The position variable takes the set of discrete values $\zeta_i = \Delta\zeta i$ for $\{i = 0, \dots, N_{\zeta}\}$. The values of k are also restricted to the discrete set $k_p = (2p - N_k - 1)\Delta k/2$ for $\{p = 1, \dots, N_k\}$. On a discrete mesh, the first derivative $\frac{\partial f_{js}}{\partial \zeta}(\zeta_i, k_p)$ is approximated by the left-hand difference for $k_p > 0$ and the right-hand difference for $k_p < 0$. It was shown In Ref. [13], that such a choice of the finite-difference representation for the derivatives leads to a stable discrete model. Projecting the equation (34) onto the finite-difference basis gives a matrix equation $\mathbf{L} \cdot \mathbf{f} = \mathbf{b}$. In the matrix \mathbf{L} , only the diagonal blocks and one upper and one lower co-diagonal blocks are nonzero:

$$\mathbf{L} = \begin{pmatrix} A_1 & -E & 0 & \dots & 0 \\ -V & A_2 & -E & \dots & 0 \\ 0 & -V & A_3 & \dots & 0 \\ \vdots & \vdots & \vdots & \ddots & \vdots \\ 0 & 0 & 0 & \dots & A_{N_{\zeta}-1} \end{pmatrix}. \quad (36)$$

Here, the $N_k \times N_k$ matrices A_i , E , and V are

$$[A_i]_{pp'} = \delta_{pp'} - \frac{2m_j^{\parallel} \Delta\zeta}{\hbar^2 (2p - N_k - 1) \Delta k} W_{js}(\zeta_i, k_p - k_{p'}),$$

$$[E]_{pp'} = \delta_{pp'} \theta \left\{ \frac{N_k + 1}{2} - p \right\}, \quad [V]_{pp'} = \delta_{pp'} \theta \left\{ p - \frac{N_k + 1}{2} \right\}, \quad (37)$$

and the vectors are

$$[f_i]_p = f_{js}(\zeta_i, k_p), \quad \text{and} \quad [b_i]_p = B_{js}(\zeta_i, k_p), \quad i = 1, N_{\zeta-1}, \quad i = 1, N_k. \quad (38)$$

A recursive algorithm is used to solve the matrix equation $\mathbf{L} \cdot \mathbf{f} = \mathbf{b}$. Invoking downward elimination, we are dealing with $B_i = (A_i - VB_{i-1})^{-1}E$ and $N_i = (A_i - VB_{i-1})^{-1}(b_i + VN_{i-1})$ ($i = 1, \dots, N_{\zeta}$) as relevant matrices and vectors. Then, upward elimination eventually yields the solution $f_i = B_i f_{i+1} + N_i$ ($i = N_{\zeta} - 1, \dots, 1$). If an index of a matrix or a vector is smaller than 1 or larger than $N_{\zeta} - 1$, the corresponding term is supposed to vanish.

In the channel, the difference between effective potentials $\mathcal{E}_{js}(\zeta)$ with different (j, s) is of the order of or larger than the thermal energy $k_B T$. Therefore, in the channel only a few lowest inversion subbands must be taken into account. In the source and drain, however, many quantum states (j, s) of the radial motion are strongly populated by electrons. Therefore, we should account for all of them in order to calculate the charge distribution. Here, we can use the fact that, according to our approximation, the current flows only through the lowest subbands in the channel. Hence, only for these subbands the partial Wigner distribution function of electrons is non-equilibrium. In other subbands electrons are maintained in the state of equilibrium, even when a bias is applied. So, in Eq. (15) for the electron density, we can substitute functions $f_{jmsms}(z, k)$ of higher subbands by corresponding equilibrium functions. Formally, adding and subtracting the equilibrium functions for the lowest subbands in Eq. (15), we arrive at the following equation for the electron density

$$n(\mathbf{r}) = n_{eq}(\mathbf{r}) + \frac{1}{2\pi} \sum_{js} \int_{-\infty}^{+\infty} dk \left[f_{js}(z, k) |\psi_{js}(r, z)|^2 - f_{js}^{eq}(z, k) |\psi_{js}^{eq}(r, z)|^2 \right], \quad (39)$$

where $n_{eq}(\mathbf{r})$ and $\psi_{js}^{eq}(r, z)$ are the electron density and the wavefunction of the radial motion in the state of equilibrium, respectively. The summation on the right-hand side of Eq. (39) is performed only over the lowest subbands. Since the electrostatic potential does not penetrate into the source and drain, we suppose that the equilibrium electron density *in these regions* is well described by the Thomas-Fermi approximation:

$$n_{eq}(\mathbf{r}) = N_C \frac{2}{\sqrt{\pi}} F_{1/2}(\beta(eV(r, z) + E_F - E_C)), \quad (40)$$

where the Fermi integral is

$$F_{1/2}(x) = \int_0^{\infty} \frac{\sqrt{t} dt}{\exp(t - x) + 1}. \quad (41)$$

Here N_C is the effective density of states in the conduction band and E_F is the Fermi level of the system in the state of equilibrium.

VI. NUMERICAL RESULTS

During the device simulation three equations are solved self-consistently: (i) the equation for the wavefunction of the radial motion (7), (ii) the equation for the partial Wigner distribution function (19) and (iii) the Poisson equation (2). The methods of numerical solution

of Eqs. (7) and (2) are the same as for the equilibrium state [12]. The numerical model for Eq. (19) was described in the previous section. In the present calculations the four lowest subbands ($j = 1, 2$ $s = 1, 2$) are taken into account. The electron density in the channel is obtained from Eq. (15), whereas in the source and drain regions it is determined from Eq. (39). The calculations are performed for structures with a channel of radius $R = 50$ nm and for various values of the length: $L_{ch} = 40, 60, 70$ and 80 nm. The width of the oxide layer is taken to be 4 nm. All calculations are carried out with $N_{\zeta} = 100$ and $N_k = 100$. The partial Wigner distribution functions, which are obtained as a result of the self-consistent procedure, are then used to calculate the current according to Eq. (16).

We investigate two cases: ballistic transport and quantum transport. The scattering of the electrons is taken into account. The distribution of the electrostatic potential is represented in Fig. 2 for $V_{ds} = 0.3$ V and $V_G = 1$ V. This picture is typical for the MOSFET structure, which is considered here. The cross-sections of the electrostatic potentials for $r = 0, 30, 40, 45, 48, 50$ nm are shown in Fig. 3. The main part of the applied gate voltage falls in the insulator ($50 \text{ nm} < r < 54 \text{ nm}$). Along the cylinder axis in the channel, the electrostatic potential barrier for the electron increases up to about 0.4 eV. Since the potential along the cylinder axis is always high, the current mainly flows in a thin layer near the semiconductor-oxide interface. This feature provides a way of controlling I_{ds} through the gate voltage. Varying V_{ds} and V_G mainly changes the shape of this narrow path, and, as a consequence, influences the form of the effective potential $\mathcal{E}_{js}(z)$. As follows from Figs. 2 and 3, the radius of the pillar can be taken shorter without causing barrier degradation. At the p-n-junctions (source-channel and drain-channel) the electrons meet barriers across the whole semiconductor. These barriers are found to persist even for high values of the applied source-drain voltage and prevent an electron flood from the side of the strongly doped source. The pattern of the electrostatic potentials differs mainly near the semiconductor-oxide interface, where the inversion layer is formed. In Fig. 4 the effective potential for the lowest inversion subband ($j = 1, s = 1$) is plotted as a function of z for different applied bias $V_{ds} = 0, \dots, 0.5$ V, $V_G = 1$ V, $L_{ch} = 60$ nm. It is seen that the effective potential reproduces the distribution of the electrostatic potential near the semiconductor-oxide interface. In the case of ballistic transport (dashed curve), the applied drain-source voltage sharply drops near the drain-channel junction (Figs. 3 and 4). The scattering of electrons (solid curve) smoothes out the applied voltage, which is now varying linearly along the whole channel. Note, *that the potential obtained by taking into account scattering is always higher than that of the ballistic case.* The explanation is clear from Fig. 5, where the linear electron density is plotted for $V_G = 1$ V and $L_{ch} = 60$ nm. It is seen that, due to scattering, the electron density in the channel (solid curve) rises and smoothes out. Hence, the applied gate voltage is screened more effectively, and as a result, the potential exceeds that of the ballistic case. It should be noted that at equilibrium ($V_{ds} = 0$) the linear density and the effective potential for both cases (with and without scattering) are equal to each other. This result follows from the principle of detailed balance.

The current-voltage characteristics (the current density $I = J/2\pi R$ vs. the source-drain voltage V_{ds}) are shown in Figs. 6 and 7 for the structures with channel lengths $L_{ch} = 40, \dots, 80$ nm. At a threshold voltage $V_{ds} \approx 0.2$ V a kink in the I - V characteristics of the device is seen. At subthreshold voltages $V_{ds} < 0.2$ V the derivative dV_{ds}/dJ gives the resistance of the structure. It is natural, that scattering enhances the resistance of the

structure (solid curve) compared to the ballistic transport (dashed curve). Scattering is also found to smear the kink in the $I-V$ characteristic. At a voltage $V_{ds} > 0.2$ V a saturation regime is reached. In this part of $I - V$ characteristics, the current through the structure increases more slowly than it does at a subthreshold voltage. The slope of the $I - V$ curve in the saturation regime rises when the length of the channel decreases. This effect is explained by a reduction of the p-n junction barrier potential as the length of the channel becomes shorter than the p-n junction width. In Fig. 7, one can see that, when the transistor is switched off ($V_G < 0.5$ V), the influence of the scattering on the current is weak. This fact is due to a low concentration of electrons, resulting in a low amplitude of the scattering processes.

In Figs. 8a and 8b the contour plots of the partial Wigner distribution function ($j = 1, s = 1$) are given for both cases (a – without and b – with scattering). The lighter regions in these plots indicate the higher density of electrons. Far from the p-n-junction, where the effective potential varies almost linearly, the partial Wigner distribution function can be interpreted as a distribution of electrons in the phase space. When electrons travel in the inversion layer without scattering, their velocity increases monotonously along the whole channel. Therefore, in the phase-space representation the distribution of ballistic electrons looks as *a narrow stream in the channel* (Fig. 8a). As it is expected, *scattering washes out the electron jet in the channel* (see Fig. 8b). It is worth mentioning that the electron stream in the channel does not disappear. It means that in this case the electron transport through the channel combines the features of both diffusive and ballistic motion.

VII. SUMMARY

We have developed a model for the detailed investigation of quantum transport in MOSFET devices. The model employs the Wigner distribution function formalism allowing us to account for electron scattering by impurities and phonons. Numerical simulation of a cylindrical nanosize MOSFET structure was performed. $I - V$ characteristics for different values of the channel length were obtained. It is shown that the slope of the $I - V$ characteristic in the saturation regime rises as the channel length increases. This is due to the decrease of the p-n junction barrier potential.

Finally, we have demonstrated that the inclusion of a collision term in numerical simulation is important for low source–drain voltages. The calculations have shown that the scattering leads to an increase of the electron density in the channel and smoothes out the applied voltage along the entire channel. The analysis of the electron phase-space distribution in the channel has shown that, in spite of scattering, electrons are able to flow through the channel as a narrow stream although, to a certain extent, the scattering is seen to wash out this jet. Accordingly, features of both ballistic and diffusive transport are simultaneously encountered.

ACKNOWLEDGMENTS

This work has been supported by the Interuniversitaire Attractiepolen — Belgische Staat, Diensten van de Eerste Minister – Wetenschappelijke, technische en culturele Aangelegen-

heden; PHANTOMS Research Network; F.W.O.-V. projects Nos. G.0287.95, 9.0193.97 and W.O.G. WO.025.99N (Belgium).

REFERENCES

- [1] Y. Nakajima, Y. Takahashi, S. Horiguchi, K. Iwadate, H. Namatsu, K. Kurihara, and M. Tabe, *Appl. Phys. Lett.* **65**, 2833 (1994).
- [2] M. Ono, M. Saito, T. Yoshitomi, C. Fiegna, T. Ohguro, and H. Iwai, *IEEE Trans. Electron. Devices*, **42**, 1822 (1995).
- [3] L. Guo, P. R. Krauss, and S. Y. Chou, *Appl. Phys. Lett.* **71**, 1881 (1997).
- [4] J. C. S. Woo, K. W. Terril and P. K. Vasudev, *IEEE Trans. Electron. Devices* **ED-37** 1999 (1990).
- [5] H. O. Joachim, Y. Yamaguchi, K. Ishikawa, Y. Inoue, and T. Nashimura, *IEEE Trans. Electron. Devices*, **40**, 1812 (1993).
- [6] S. Pidini and M. Koyanagi, *Jpn. J. App. Phys.* **37** 1264 (1998).
- [7] R. Koh and H. Kato, *Jpn. J. App. Phys.* **34** 836 (1995).
- [8] H. O. Joachim, Y. Yamaguchi, Y. Inoue and N. Tsubouchi, *Jpn. J. App. Phys.* **34** 822 (1995).
- [9] O. Arisumi, K. Matsuzawa, N. Shiguyo, M. Terauchi, A. Nishiyama and Yoshimi, *Jpn. J. App. Phys.* **35** 992 (1996).
- [10] T. Sekigawa, Y. Hayashi, *Solid State Electronics*, **27**, 827 (1984).
- [11] F. G. Pikus and K. K. Liharev, *Appl. Phys. Lett.* **71**, 3661 (1997).
- [12] E. P. Pokatilov, V. M. Fomin, S. N. Balaban, V. N. Gladilin, S. N. Klimin, J. T. Devreese, W. Magnus, W. Schoenmaker, N. Collaert, M. Van Rossum, and K. De Meyer, *J. Appl. Phys.* **85**, 6625 (1999).
- [13] W. Frensley, *Rev. Mod. Phys.* **62**, 745 (1990).
- [14] H. Tsuchiya, M. Ogawa and T. Miyoshi, *Jpn. J. Appl. Phys.* **30**, 3853 (1991).
- [15] K. L. Jensen and A. K. Ganguly, *J. Appl. Phys.* **73**, 4409 (1993).
- [16] A. Isihara, *Statistical Physics*, State University of New York, Buffalo, Academic Press (New York – London, 1971).
- [17] A. Abramowitz, L. A. Stegun (Eds.), *Handbook of Mathematical Functions with Formulas, Graphs, and Mathematical Tables* (National Bureau of Standards, Washington, DC, 1972).
- [18] *Semiconductors. Physics of II-VI and I-VII Compounds, Semimagnetic Semiconductors*, edited by K. H. Hellwege, Landolt-Börnstein, New Series, Group III, Vol. 17, (Springer, Berlin, 1982).

FIGURE CAPTIONS

Fig. 1. Scheme of the cylindrical nanosize MOSFET.

Fig. 2. Distribution of the electrostatic potential in the MOSFET with $L_{ch} = 60$ nm at $V_G = 1$ V and $V_{ds} = 0.3$ V.

Fig. 3. Cross-sections of the electrostatic potentials without scattering (dashed curves) and with scattering from acceptor impurities and from an acoustic deformation potential (solid curves).

Fig. 4. Effective potential as a function of z for various V_{ds} , $L_{ch} = 60$ nm.

Fig. 5. Linear electron density in the channel as a function of z for various V_{ds} , $L_{ch} = 60$ nm.

Fig. 6. Current-voltage characteristics at $V_G = 1$ V for different channel lengths.

Fig. 7. Current-voltage characteristics for MOSFET with $L_{ch} = 40$ nm.

Fig. 8. Contour plots of the partial Wigner distribution function $f_{js}(z, k)$ for the lowest subband ($j = 1, s = 1$) at $V_G = 1$ V, $V_{ds} = 0.3$ V, $L_{ch} = 60$ nm: a – without scattering, b – with scattering.

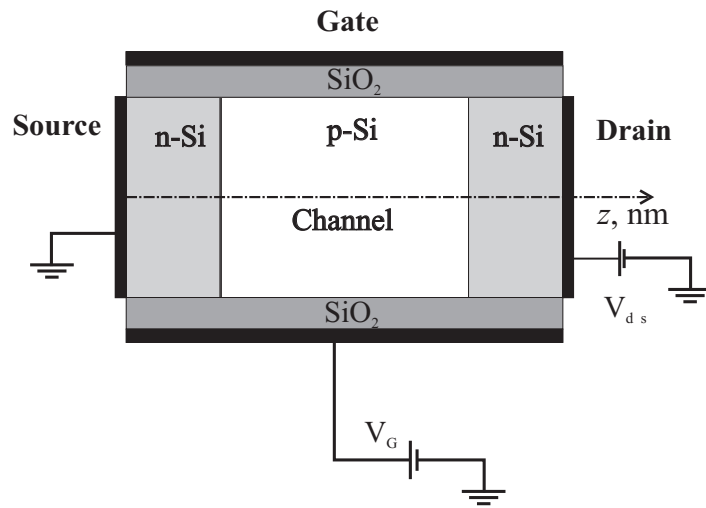


Fig. 1

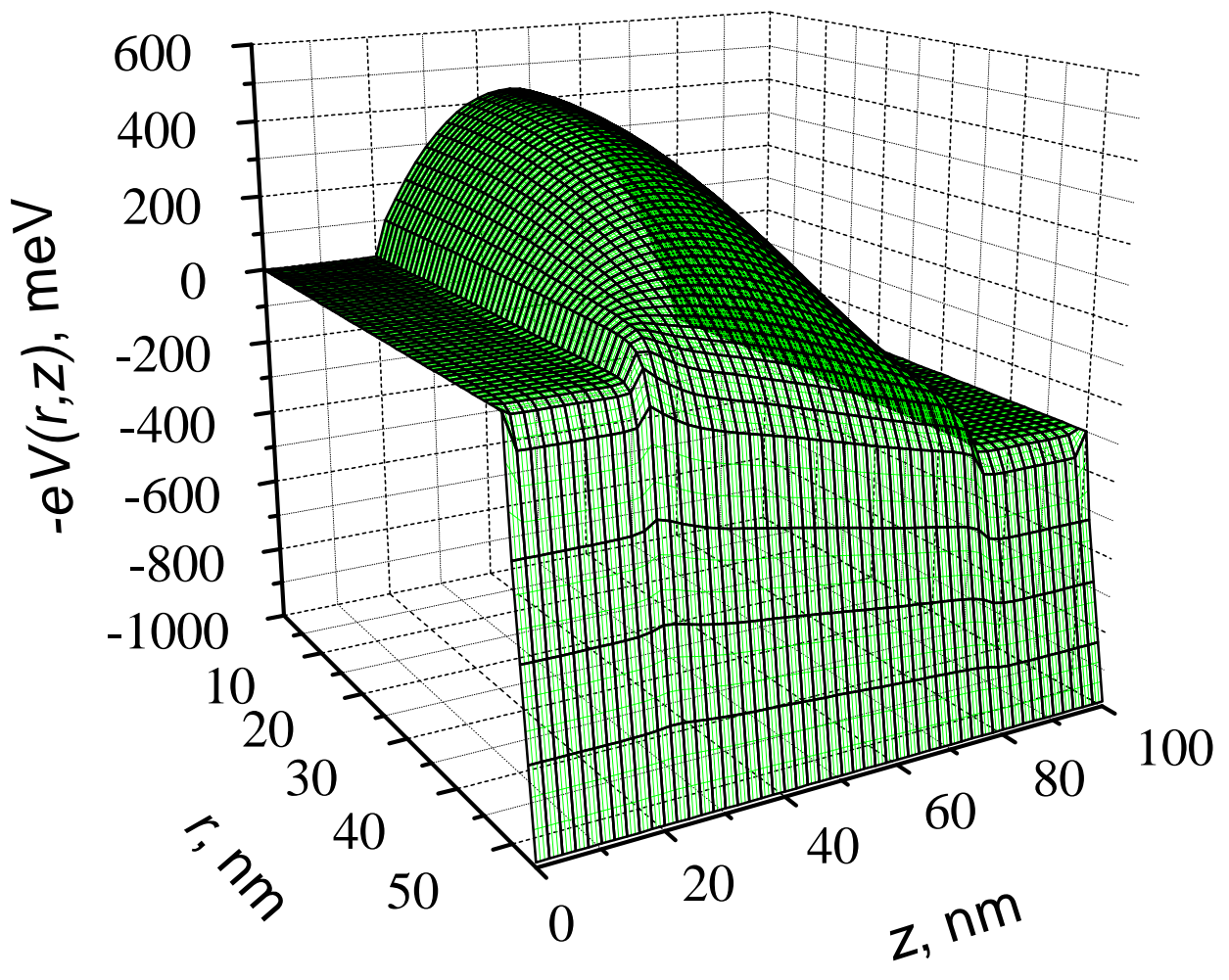


Fig. 2

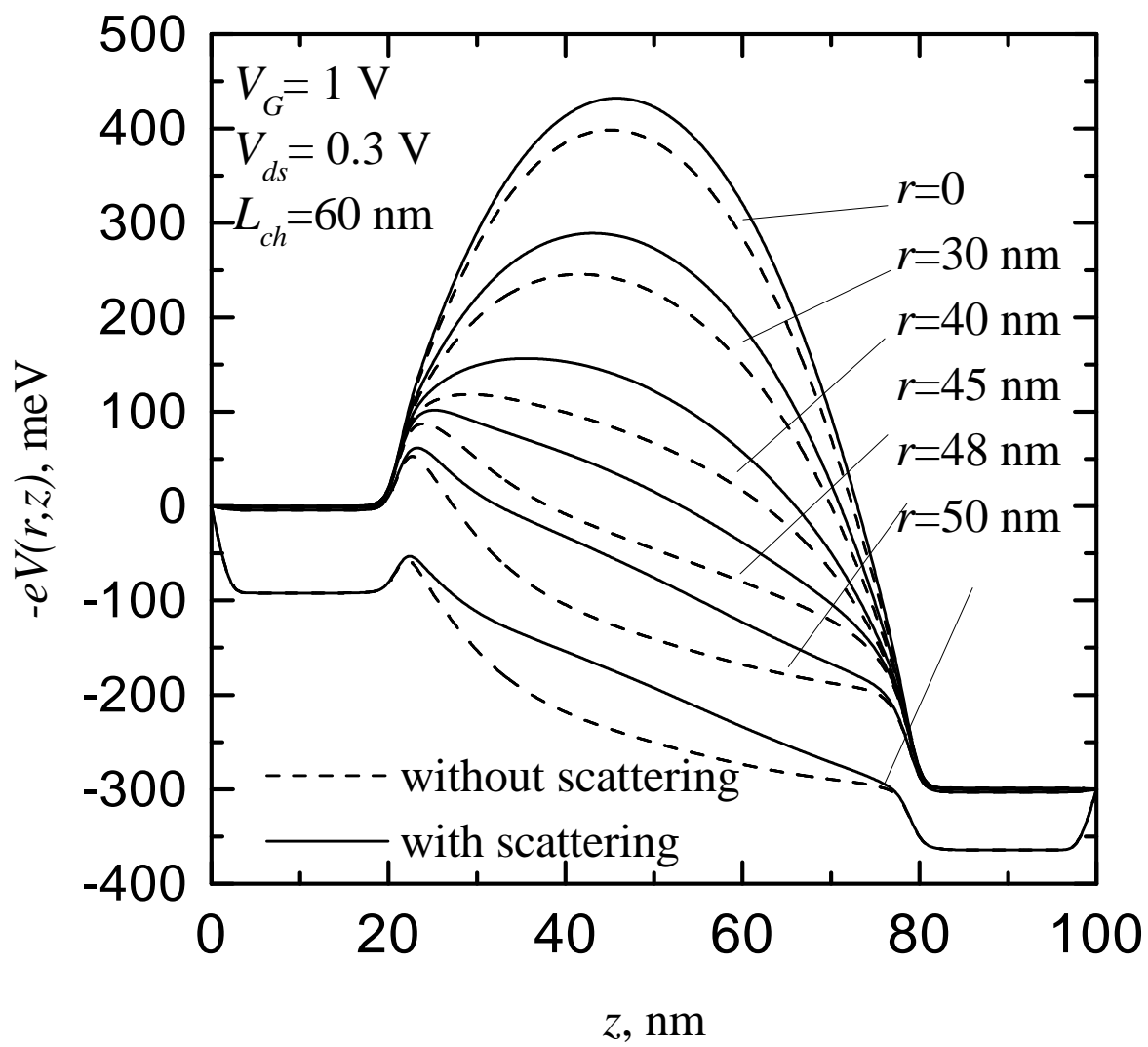


Fig. 3

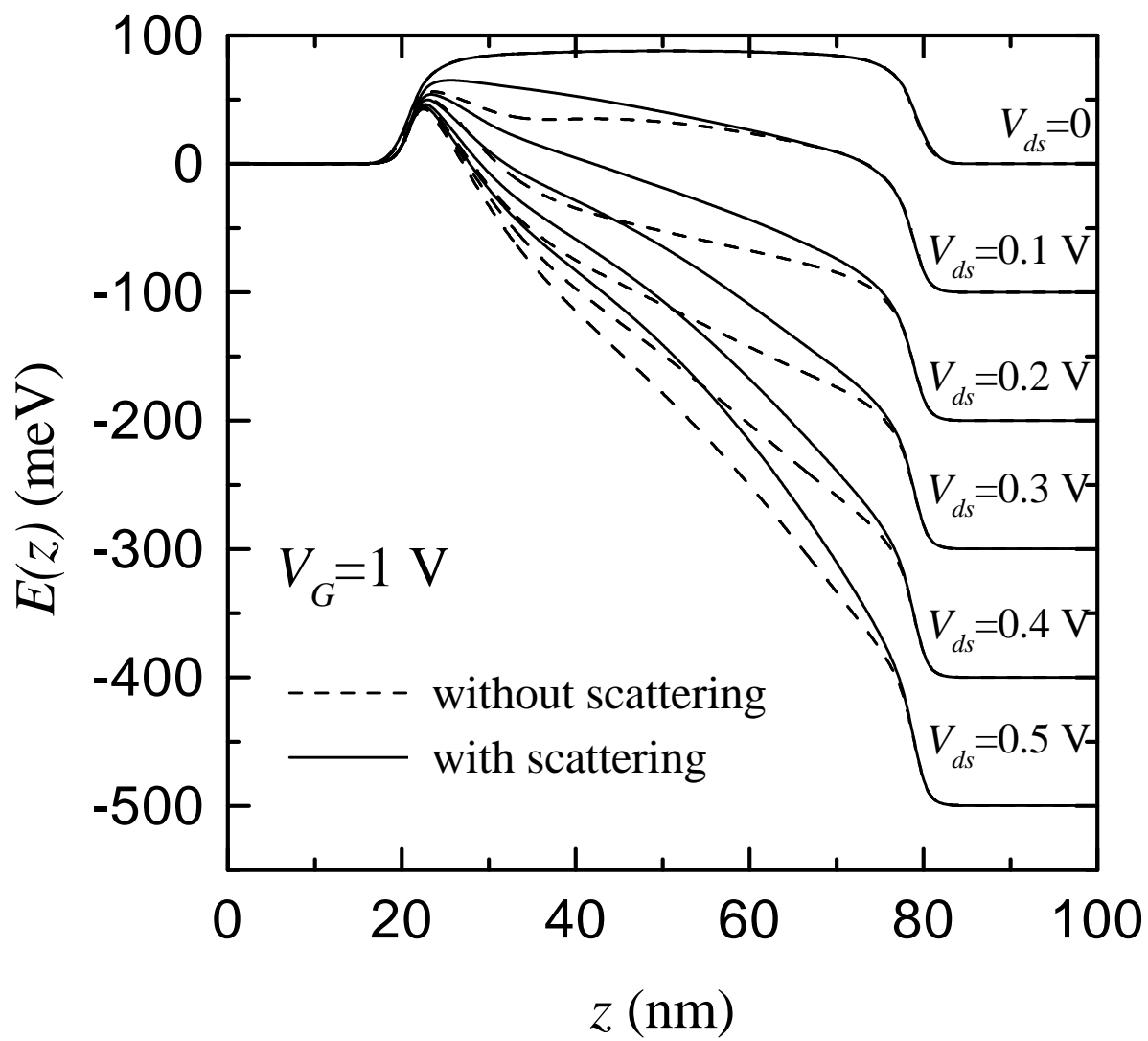


Fig. 4

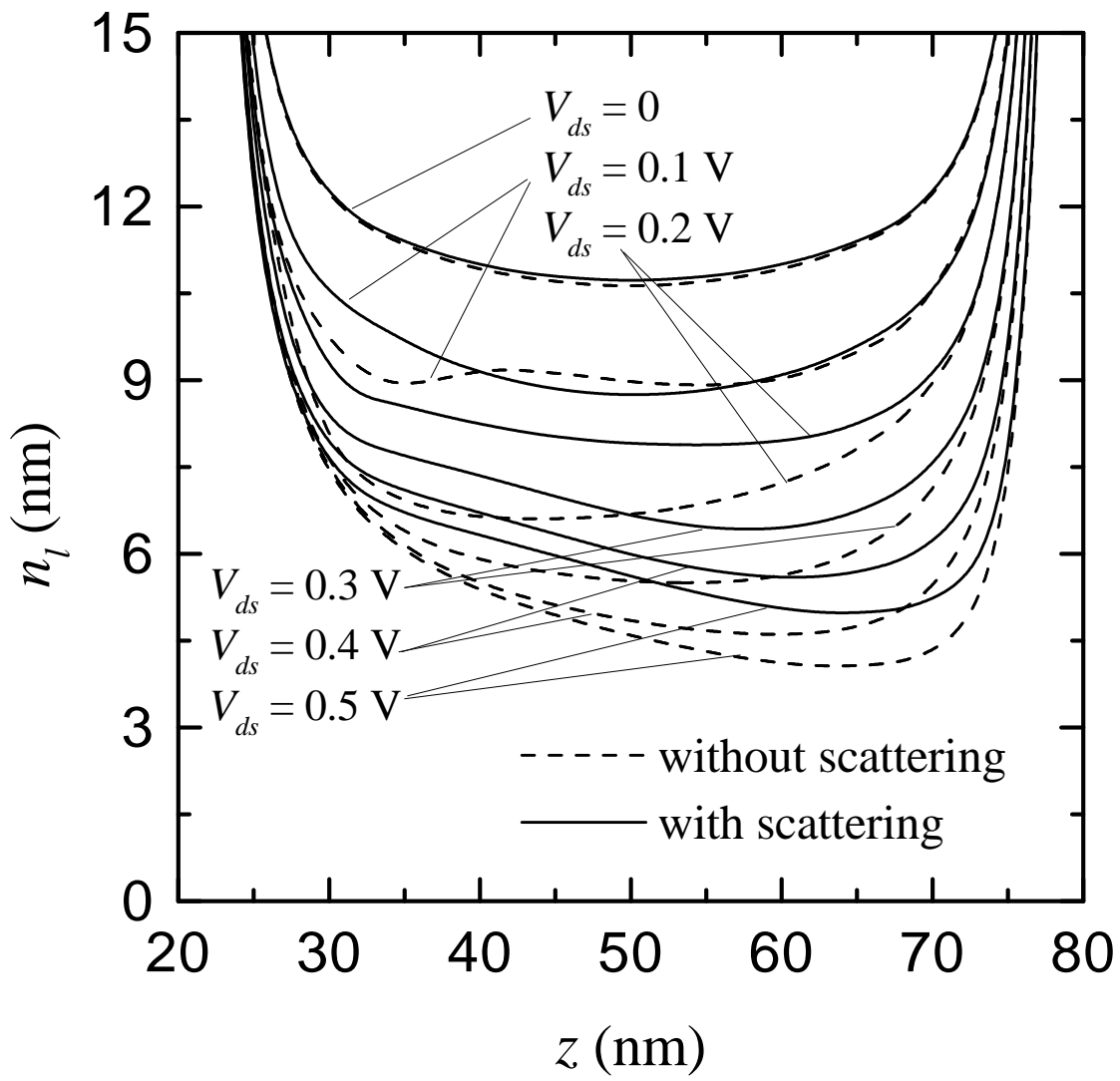


Fig. 5

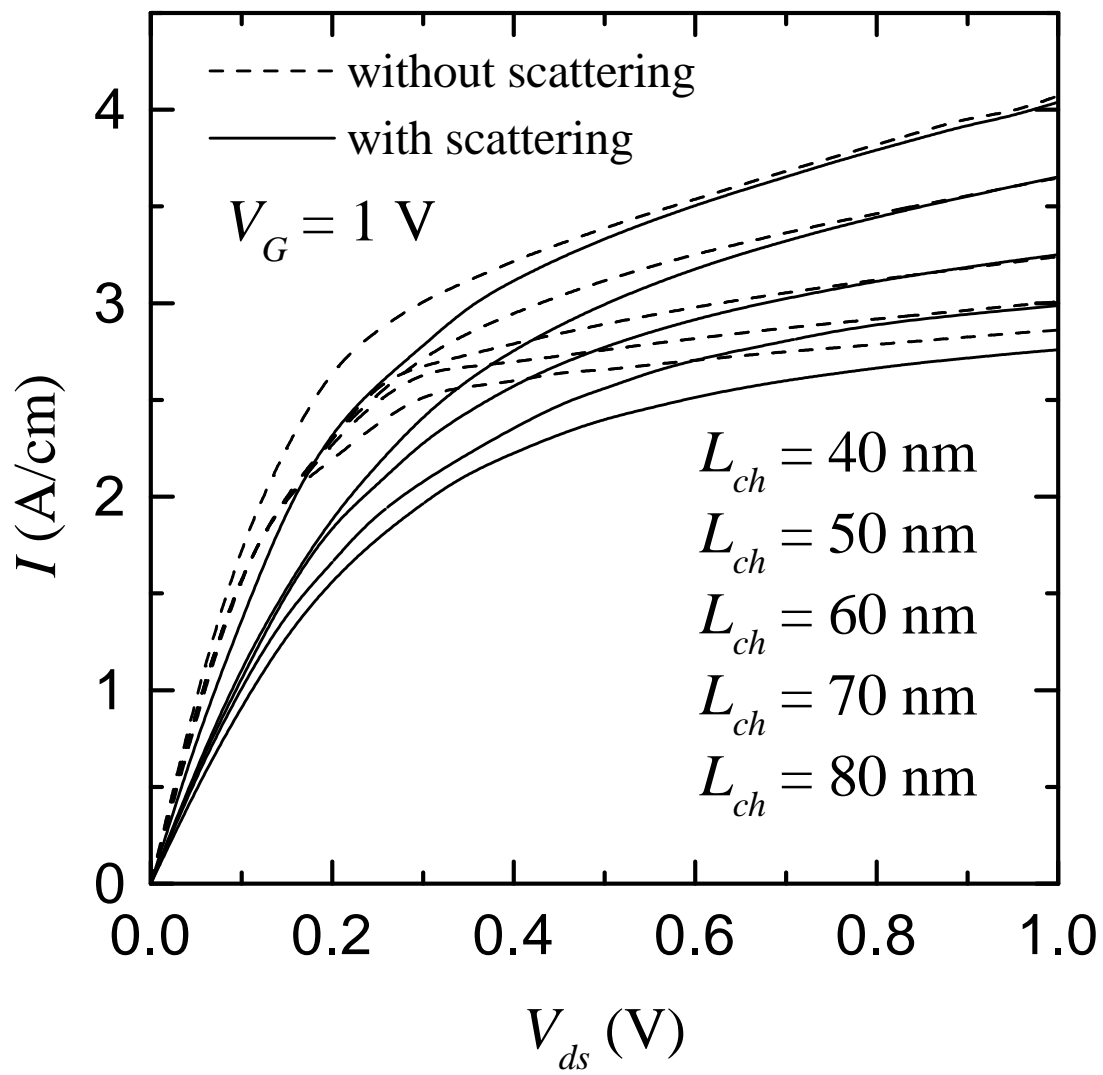


Fig. 6

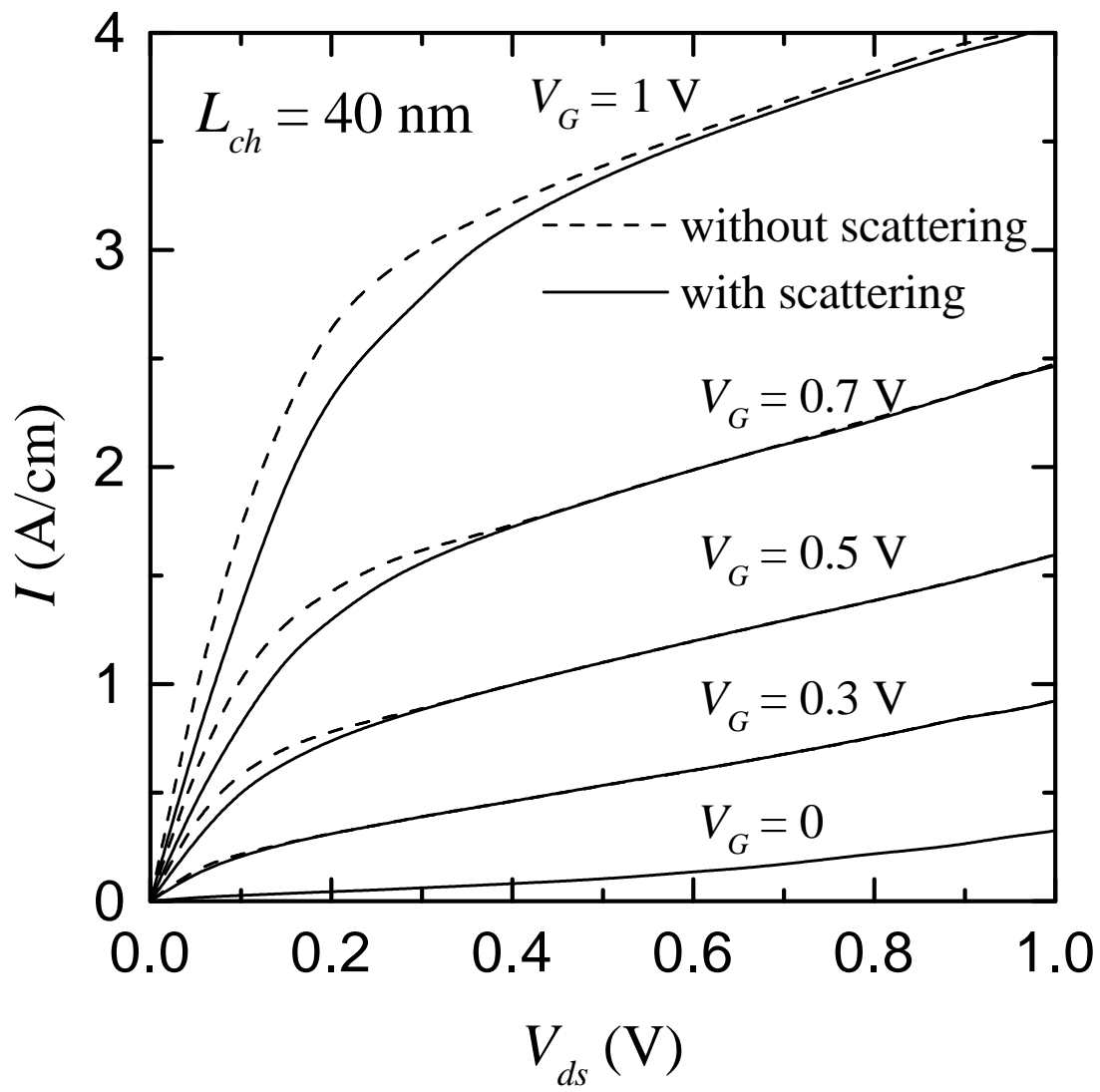


Fig. 7

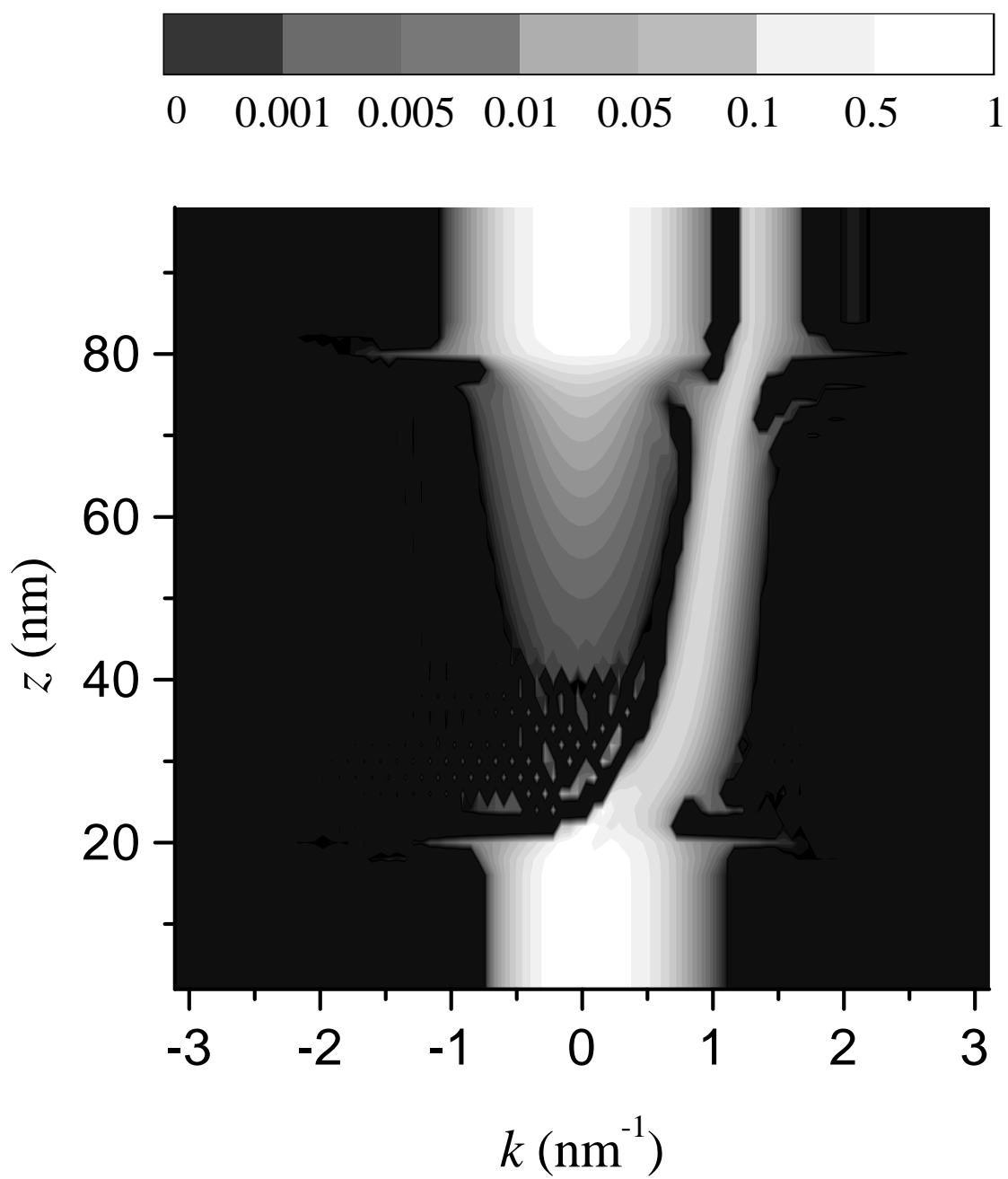


Fig. 8a

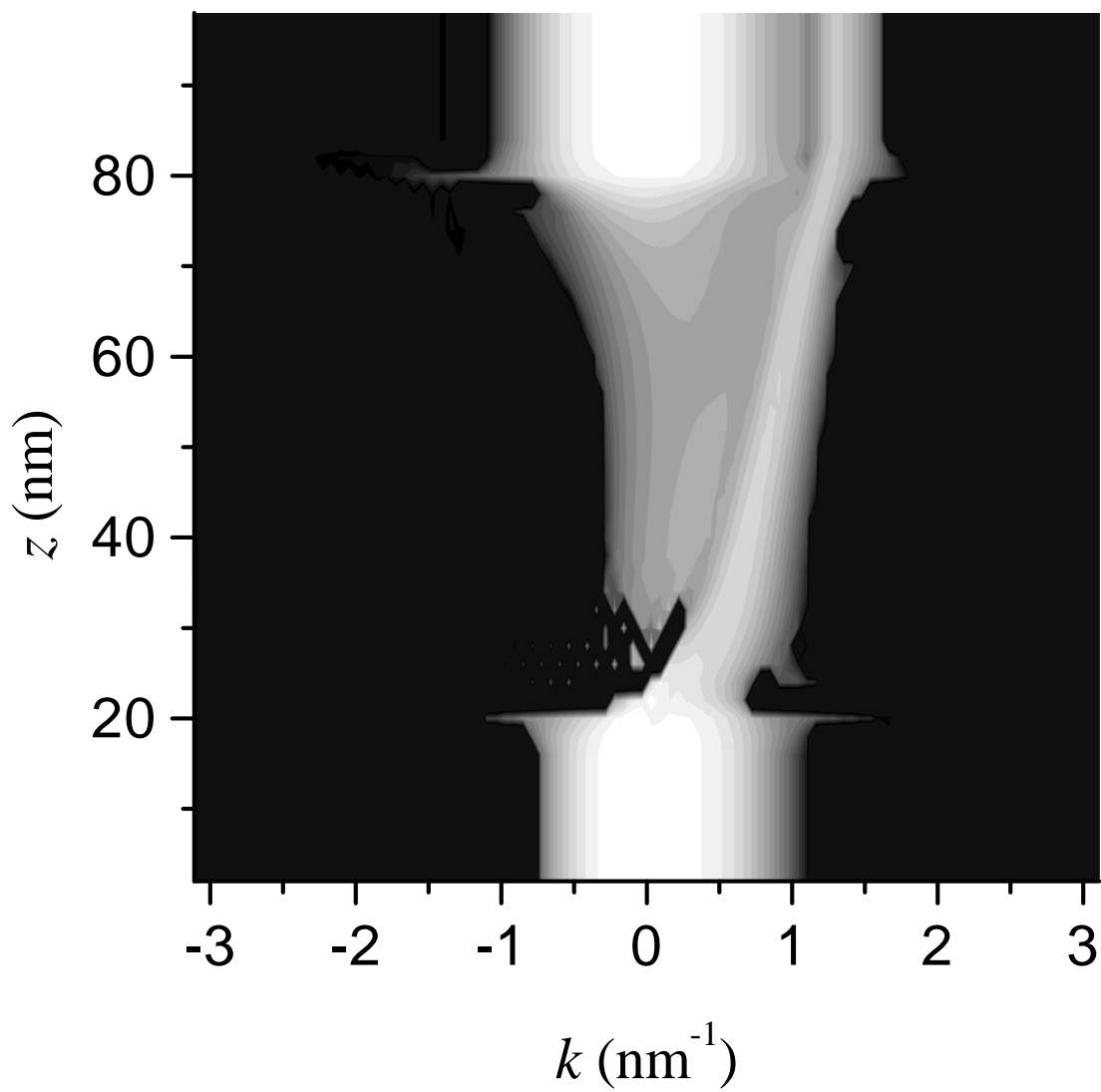


Fig. 8b